Journal of Power Sources 194 (2009) 830–834

Contents lists available at ScienceDirect

Journal of Power Sources

journal homepage: www.elsevier.com/locate/jpowsour

Short communication

First-principles investigation of the bonding, optical and lattice dynamical properties of CeO_2

Siqi Shi[a,b,*], Xuezhi Ke[c], Chuying Ouyang[d,1], Hua Zhang[a], Hangchen Ding[a], Yuanhao Tang[a], Weiwei Zhou[a], Peijuan Li[a], Minsheng Lei[d], Weihua Tang[a]

[a] Department of Physics, Center for Optoelectronics Materials and Devices, Zhejiang Sci-Tech University, Xiasha College Park, Hangzhou 310018, China
[b] State Key Laboratory of High Performance Ceramics and Superfine Microstructure, Shanghai Institute of Ceramics, Chinese Academy of Sciences, Shanghai 200050, China
[c] Department of Physics, East China Normal University, Shanghai 200062, China
[d] Department of Physics, Jiangxi Normal University, Nanchang 330022, China

ARTICLE INFO

Article history:
Received 2 April 2009
Received in revised form 10 June 2009
Accepted 11 June 2009
Available online 18 June 2009

Keywords:
Ceria
Bonding nature
Optical properties
Lattice dynamics
First-principles calculations

ABSTRACT

Bonding, optical and lattice dynamical properties of CeO_2 are investigated using first-principles density-functional theory taking into account the on-site Coulomb interaction within the LDA + U scheme. Results of the charge-density and electron-localization function distributions indicate that the bonding nature in CeO_2 is covalent bonding between Ce and O atoms. Calculated dielectric constants, Born effective charge tensors, phonon dispersion curves are in agreement with available experimental data.

1. Introduction

Ceria (CeO_2) is a technologically important oxide material with numerous applications. For example, it is extensively used in automotive three-way catalysts (TWCs) to remove combustion exhaust such as NO_x, CO, and hydrocarbons [1–3] and in the future hydrogen production and purification technology [4,5]. These technological applications are strongly related with the facility of formation and transportation of oxygen vacancies in CeO_2. The high dielectric constant and small lattice mismatch to Si (~0.35%) make CeO_2 suitable for the future microelectronic applications such as silicon-on-insulator structures [6].

Knowledge of fundamental physical properties of this rare-earth oxide is essential to the development of those applications mentioned above. There are some experimental studies [7–10] on the bonding nature in CeO_2 and the occupation of the Ce-4f orbital. In most cases, the Anderson impurity model [11] is used to analyze the experimental data, while two opposite opinions are presented with respect to the occupation of Ce-4f orbital. Fujimori [8] and Normand et al. [9] proposed that the Ce-4f electron in CeO_2 is in a mixed-valence state with an occupation of 0.5. However, similar experimental measurements by Wuilloud et al. [10] indicate that the Ce-4f orbital in CeO_2 is almost unoccupied and the Ce ions are in the +4 valence state. Consequently, depending on the different opinion regarding the occupation of the Ce-4f orbital, different pictures about the bonding nature in CeO_2 have been presented; ionic bonding and covalent bonding. The lattice dynamical property of CeO_2 is another important issue, which has been investigated only by a few experimental and theoretical studies. Experimentally, the phonon frequencies at the Γ point have been measured by using infrared reflectivity techniques [7,12,13]. The inelastic neutron scattering experiments by Clausen et al. [14] reported the phonon frequencies below 500 cm^{-1}. To the best of our knowledge, only Yamamoto et al. [15] have done some first-principles' calculations on the lattice dynamical properties of CeO_2. Their work is performed within the local density approximation (LDA), using ultrasoft pseudopotentials and plane-wave basis sets.

In spite of the existence of the controversy about the bonding nature as mentioned above and the practical importance of CeO_2, first-principles' investigations on this compound are rarely seen in the literature. One reason for this situation could be the difficulty to provide a reasonable description of the Ce-4f state within the traditional density-functional theory (DFT). However, for the systems containing multivalent metals, in particular lanthanide species, an

* Corresponding author. Tel.: +86 571 86843222; fax: +86 571 86843222.
E-mail addresses: siqishi@yahoo.com (S. Shi), cyouyang@hotmail.com (C. Ouyang).
[1] Tel.: +86 791 8120370; fax: +86 791 8120370.

0378-7753/$ – see front matter © 2009 Elsevier B.V. All rights reserved.
doi:10.1016/j.jpowsour.2009.06.031

accurate description of the ground-state properties requires consideration of the strong correlation effect among the f electrons. In this current paper, using the DFT with the inclusion of on-site Coulomb interaction, we present systematic investigations of the bonding, optical and lattice dynamical properties of CeO_2 and make a comparison with the available experimental and theoretical results.

2. Computational details

Calculations are performed using the frozen-core all electron projected augmented wave (PAW) method [16], as implemented in the Vienna *ab inito* simulation package (VASP) [17,18]. The Ce 5s, 5p, 5d, 4f, and 6s electrons, and the O 2s and 2p electrons are treated as valence electrons. The electron exchange and correlation are treated within the local density approximation (LDA) [19]. Furthermore, in order to account for the strong on-site Coulomb repulsion among the Ce 4f electrons, a Hubbard parameter U is added to the LDA functional (LDA + U) employing the rotationally invariant approach formulated by Dudarev et al. [20], in which only the difference ($U_{\text{eff}} = U - J$) is effective. We set U_{eff} to 5.3 eV as suggested by Silva et al. [21], which is calculated self-consistently by Fabris et al. [22] using the linear-response approach of Cococcioni and de Gironcoli [23]. Since CeO_2 is experimentally known to be paramagnetic [24], only non-spin polarized calculations are performed. We use a plane-wave cutoff energy of 500 eV and $4 \times 4 \times 4$ Monkhorst–Pack k-point mesh [25] with Gaussian smearing of 0.20 eV [26]. For accurate calculation of the electronic density of states (DOS), we apply $8 \times 8 \times 8$ k-point mesh and the modified tetrahedron method of Blöchl [27]. These parameters assure a total energy convergence of 0.01 meV atom^{-1}.

To calculate the phonon dispersion, we use a direct *ab initio* force-constant approach, which was implemented by Parlinski et al. [28]. In this method, a specific atom is displaced to induce forces, which are calculated via the Hellmann–Feynman theorem, that act on the surrounding atoms. The forces are collected to form the force-constant matrices and dynamical matrices. The dynamical matrices are solved by a direct method based on the harmonic approximation [28]. In order to avoid the interaction between the two images of the displaced atoms due to the periodical boundary condition, it is necessary to use a relatively large supercell for the calculations of the force matrices. Therefore, a $2 \times 2 \times 2$ crystallographic unit cell (96 atoms) is used in the present work and in such a way the force matrix is closest to a spherical shape.

Generally speaking, the infrared optical modes at the Γ point are normally split into the longitudinal optical (LO) modes and transversal optical (TO) modes (LO/TO splitting) due to long-range Coulomb interaction. As pointed out by Kunc and Martin [29], the LO/TO splitting at the Γ point cannot be directly calculated by the direct approach, and only the TO mode is obtained without further approximation. One solution is to use an elongated supercell to recover this mode. However, due to the limited computational capability, this choice is not feasible for us in the current system. Alternatively, a non-analytical dynamical matrix can be taken into account approximately. The following matrix is responsible for the LO/TO splitting:

$$\Delta D_{ij,\alpha\beta}(\boldsymbol{q} \to 0) = \frac{4\pi e^2}{\varepsilon V \sqrt{M_i M_j}} \frac{(\boldsymbol{q} \cdot Z_i^*)_\alpha (\boldsymbol{q} \cdot Z_j^*)_\beta}{|\boldsymbol{q}|^2}, \quad (1)$$

where $\boldsymbol{q}$ is the wave vector, ε is the optical macroscopic dielectric function, V is the volume of the primitive unit cell, M_i and Z_i^* are the mass and the Born effective charge tensor of the i^{th} atom and α and β are the Cartesian indices.

Table 1
Calculated equilibrium lattice parameter a_0 (Å), bulk modulus B_0 (GPa), its pressure derivative B_0', and elastic constants (GPa) of CeO_2 compared to other theoretical and experimental values. (GGA, generalized gradient approximation; FP LMTO, full potential linear muffin tin orbital; PP, plane-wave pseudopotential method; PAW, projector augmented wave method; SIC, self-interaction corrected; LSD, local spin density approximation).

a_0	B_0	B_0'	C_{11}	C_{12}	C_{44}	Method
5.400	211.111	4.417	354.790	139.272	51.195	Present work
5.405						PP LDA [15]
5.40	210					PAW LDA + U [21]
5.37	201					PAW LDA [21]
5.39	214.7					FP LMTO [30]
5.45	193.5					PAW GGA [31]
5.366	210.1	4.4	386	124	73	PP LDA [32]
5.384	176.9					SIC LSD [33]
5.421						PP GGA [34]
			450	117	57	Shell Model [14]
5.411	220	4.4				Expt. [33]
	204		403	105	60	Expt. [35]
5.411	236	4.4				Expt. [36]
5.406	230	4.0				Expt. [37]

3. Results and discussion

3.1. Electronic structure

Bulk CeO_2 has the fluorite structure with the space group Fm-3m. Table 1 summarizes its calculated equilibrium lattice parameter a_0, bulk modulus B_0, pressure derivative of bulk modulus B_0', and elastic stiffness constants together with other theoretical and experimental ones [14,15,21,30–37]. Our calculations give an equilibrium lattice parameter of 5.400 Å, which is close to the experimental value [33,36,37]. The bulk modulus and its pressure derivative are calculated by fitting to the third order Birch–Murnaghan equation of state [38], and the results agree well with the experimental observations. Within the LDA + U approach, our calculated elastic stiffness constants are in reasonable accordance with the experimental ones of Nakajima et al. [35], which are obtained from Brillouin scattering measurements.

Fig. 1 shows the local partial density of states (LPDOS) of bulk CeO_2. The highest occupied valence band is mainly ascribed to the O-2p accompanying with some contribution from the Ce-4f and 5d, whereas the narrow empty band is located just above the Fermi level is mostly attributed to Ce-4f states. The width of the O-2p band (4.15 eV) is in good agreement with experiment [10,39] as well as previous calculations [30,40]. The respective energy gaps between the O-2p valence band top and the unoccupied Ce-4f and Ce-5d band bottoms are 2.377 and 5.186 eV, which are in reasonable agreement with the experimental values of 3.0 and 6.0 eV [10]. Here some

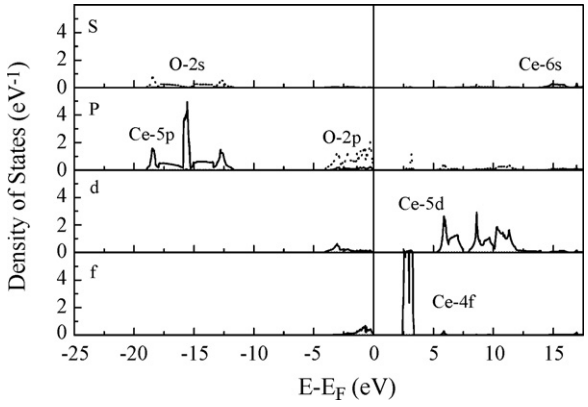

Fig. 1. Partial DOSs of states of the bulk CeO_2. Solid and dotted curves represent the partial DOSs of Ce and O, respectively.

of the earlier DFT calculations have given 2.5 and 5.5 eV (FP LMTO) [41], 1.8 and 5.7 eV (PAW GGA) [31], 2.4 and 5.3 eV (PAW LDA + U) [21]. Note that the underestimation of the energy gap is a common feature of the LDA or LDA + U calculation. Nevertheless, the calculations can explain that CeO_2 is a pronounced wide gap insulator, which is consistent with the experiment [10]. All these above mentioned structural and electronic results obtained from our present work strongly indicate that our model and LDA + U calculations are reasonable.

We now focus on the bonding nature in CeO_2. The DOS plot in Fig. 1 shows that there exists some Ce-5d and Ce-4f characters in the O-2p states. This result was also obtained in the calculations by Koelling et al. [40] and was interpreted as a justification of the partial occupation of the Ce-4f states. Therefore, the fact that there is a nonzero Ce-4f and Ce-5d density of states (DOSs) within the O-2p band provides some evidence of the covalent bonding nature of Ce-O bonds in CeO_2.

To get further insight into the bonding nature in CeO_2, we plot the valence electron density distribution because the existence of strong hybridization between states of Ce and O is direct evidence of covalent bonds between these atoms. The (1 1 0) plane with the valence electron density distribution typical for CeO_2 is shown in Fig. 2(a), from which the remarkable charge distribution overlap between Ce and O atoms is observed. This indicates the existence of substantial Ce-4f(5d)/O-2p orbital hybridization.

On the other hand, it is known that the electron-localization function (ELF) [42] is a ground-state property that discriminates in a quantitative way between different kinds of bonding. In the implementation for density-functional theory, the ELF is defined as $[1+(D/D_h)^2]^{-1}$, where D is the excess of local kinetic energy due to the Pauli principle. Thus D can be obtained from $\tau - t_W$, with τ being the Kohn–Sham local kinetic energy, $\tau = 1/2\sum|\nabla\varphi_i|^2$, where φ_i are the Kohn–Sham orbitals, and t_W is the value of τ without the inclusion of the Pauli principle ($\sim|\nabla\rho|^2/\rho$, ρ being the charge-density). D_h represents D for the corresponding uniform electron gas ($\sim\rho^{5/3}$). According to this definition the ELF can have values between 0 and 1, where 1 corresponds to perfect localization. In Fig. 4(b) the ELF is shown for the same plane as considered above for the charge-density distribution. Remarkably, the shared-electron picture between the Ce and O atoms, characteristic for covalent bonds, is seen in the ELF. Thus the covalent nature of Ce-O bonding is confirmed by our ELF analysis. In any case, the present theoretical calculations reproduce the experimental results reported by using the optical reflectivity technique [7] very well.

3.2. Born effective charges and optical properties

As mentioned in the methodological section that the Coulomb interaction affects the LO/TO splitting at the Γ point. This interaction is directly related to the Born effective charge tensors, e.g., a finite dipole moment of p is created by the displacement ($\Delta\boldsymbol{u}$) of the ith atom,

$$\boldsymbol{p} = Z^*_{i,\alpha,\beta} \times \Delta\boldsymbol{u}, \tag{2}$$

where $\boldsymbol{p} = Z^*_{i,\alpha,\beta} \times \Delta\boldsymbol{u}$ is the Born effective charge tensor, and $\Delta\boldsymbol{u}$ is the displacement of the ith atom in the unit cell. According to the polarization theory [43,44], the total difference in polarization between the distorted and undistorted structures is given by:

$$\Delta\boldsymbol{P} = \Delta\boldsymbol{P}_{\mathrm{e}} + \Delta\boldsymbol{P}_{\mathrm{ion}}, \tag{3}$$

where $\Delta\boldsymbol{P}_{\mathrm{e}}$ is the electronic contribution obtained from the Berry-phase polarization approach [44], and $\Delta\boldsymbol{P}_{\mathrm{ion}}$ is the ionic contribution by:

$$\Delta\boldsymbol{P}_{\mathrm{ion}} = \frac{|e|z_i\Delta\boldsymbol{u}}{V}, \tag{4}$$

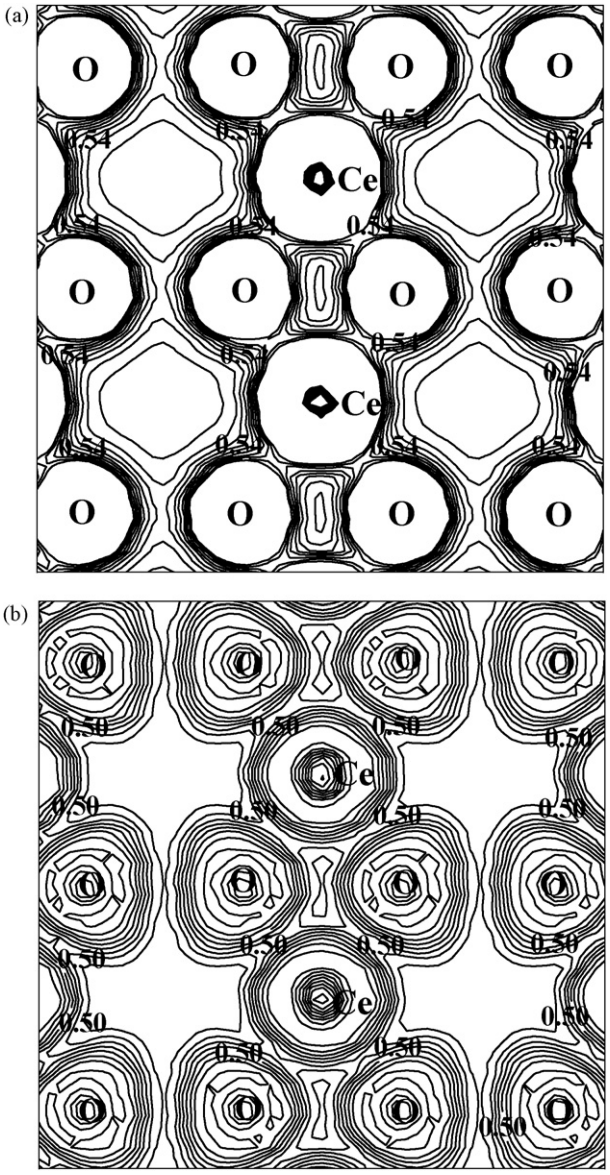

Fig. 2. Valence electron density distribution (a) and electron-localization function (b) on the (110) plane of CeO_2. In (a), contours are plotted from 0.0 to 0.6 eÅ^{-3} with a spacing of 0.06 eÅ^{-3}. In (b), contours are plotted from 0.0 to 1.0 with a spacing of 0.1. The horizontal and vertical axes are depicted by the [0 0 1] and [1–10] directions, respectively.

where z_i is the valence atomic number of the i^{th} atom, V is the volume of the unit cell, and $\Delta\boldsymbol{u}$ is the displacement of the i^{th} atom in the unit cell. Once $\Delta\boldsymbol{P}$ is known, the Born effective charge tensor for the β component can be obtained from the following formula:

$$i, \alpha, \beta_* = \frac{\boldsymbol{V}}{|e|}\frac{(\Delta\boldsymbol{P})_\alpha}{\Delta\boldsymbol{u}}, \tag{5}$$

where α denotes the direction of the polarization. In the Berry-phase calculations, we chose the displacement to be 0.05 Å, and use a set of strings of 6-k points parallel to some chosen reciprocal lattice vectors d to calculate the electronic polarization. With these settings, we found the results are well converged.

In CeO_2, Ce and O reside at 4a and 8c Wyckoff positions, respectively. Thus, the Born effective charge tensors for both atoms are isotropic and diagonal due to the high symmetry of Fm-3m, i.e. $Z^*_{ij} = Z^*\delta_{ij}$ for each atom. The calculated Born effective charges are $Z^*_{Ce} = 5.4794$ and $Z^*_O = -2.7397$, respectively. The satisfaction of

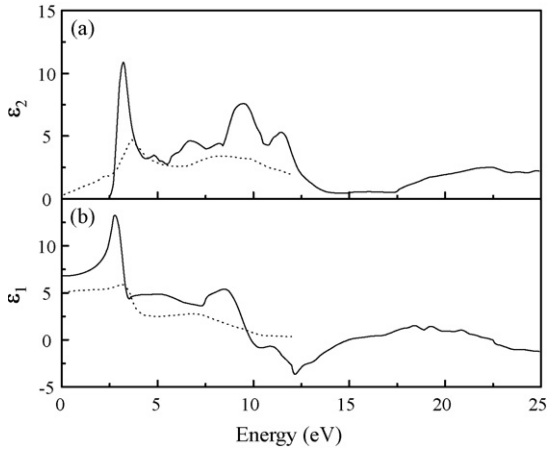

Fig. 3. Calculated imaginary part $\varepsilon_2(\omega)$ (a) and real part $\varepsilon_1(\omega)$ (b) of the dielectric function of CeO_2. The dotted lines represent the experimental results taken from Ref. [7].

the acoustic sum rule ($\sum Z^* = 0$) indicates the calculation for the effective charges is very well converged. The present values are in reasonable agreement with those ($\boldsymbol{Z}^*_{Ce} = 5.712$ and $Z^*_O = -2.856$) calculated from a similar pseudopotential plane-wave LDA method [15].

Figs. 3 and 4 show some optical properties of CeO_2 such as the imaginary [$\varepsilon_2(E)$] and real [$\varepsilon_1(E)$] parts of the dielectric function, as well as the reflectivity. For the purpose of the comparison, the experimental data by Marabelli and Wachter [7], who have carried out reflectivity measurements with CeO_2 single crystals samples, are presented in dotted lines. It is seen that the experimental curves show a sharp peak at about 3.66 eV and a wide peak at about 8.46 eV. The calculated ε_2 curve in Fig. 3(a) shows a sharp increase at about 3.2 eV at the first onset of the optical transitions. The second main peak is situated at about 9.5 eV and the third one at 22.3 eV. Thus the theoretical curve reveals a similar structure, reproducing the experimental behavior [7] very well.

The intensities obtained from the experiments are smaller than that from our calculations. The reason behind this difference in intensity could lie in the difference in the broadening of the experimental and theoretical curves. Generally speaking, larger smearing widths lead to lower intensities and thus the heights of the peaks are lower. As the value of the broadening is not reported in those experimental papers, it is hard to compare with our results. For the present calculations, Gaussian smearing with an energy width of 0.1 eV has been used.

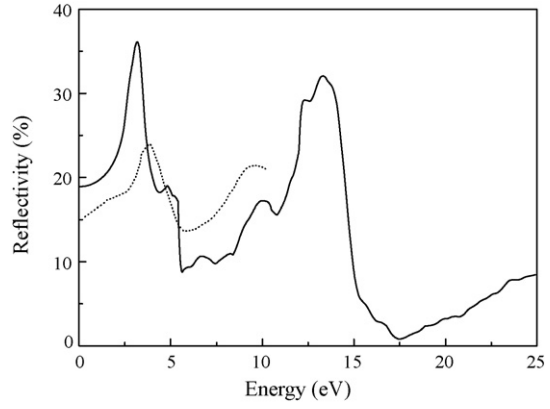

Fig. 4. Calculated reflectivity of CeO_2. The dotted line represents the experimental result taken from Ref. [7].

Table 2
Calculated static dielectric constant (ε_0), Γ point Raman (ω_R), infrared ($\omega_{l,\,TO}$ and $\omega_{l,\,LO}$) phonon frequencies compared to other theoretical and experimental values.

ε_0	ω_R (cm^{-1})	$\omega_{l,TO}$ (cm^{-1})	$\omega_{l,LO}$ (cm^{-1})	Method
6.791	439.711	301.548	590.190	Present work
7.5		305		Calc. [15]
4.7		218	597	Expt. [7]
5.31		272	595	Expt. [12]
6.0		283		Expt. [13]
2.85	443	270		Expt. [14]
6.0				Expt. [45]
3.0				Expt. [46]

In Fig. 3(a) the peaks of $\varepsilon_2(E)$ originate from inter-band transitions from valence band states to conduction band states. According to the dipolar selection rule, only transitions that change the angular momentum quantum number l by unity ($\Delta l = 1$) are allowed. Consistent with the DOSs of CeO_2 (see Fig. 1), the first peak in ε_2 at about 3 eV is explained as the transition from Ce-5d to Ce-4f states, while the second peak corresponds to the Ce-5p → Ce-5d transition. A remarkable fact regarding the first peak in $\varepsilon_2(E)$, also pointed out in Ref. [7], is that its width is essentially determined by the width of the highest occupied valence band of CeO_2 (about 4 eV, Fig. 1). Moreover, the complicated structure of this peak in $\varepsilon_2(E)$ is similar to the fine structure of the DOSs in the energy interval from −4 eV to Fermi level.

Fig. 3(b) shows the real part $\varepsilon_1(E)$ of the dielectric function obtained by means of a Kramers–Kronig transformation together with the experimental result from reference [7]. The shape of the calculated curve exhibits the same main features as the experimental results. The peak at about 2.8 eV corresponds to the experimental one at 3.12 eV, and the second broad peak of $\varepsilon_1(E)$ is situated at about 8.5 eV, corresponding to the experimental peak at 7.32 eV. Near the intrinsic gap, the real part of the dielectric constant is enhanced in comparison with experiments. Our calculation gives a value of about 6.7 for the static dielectric constant, whereas the experimental ones are 4.7 (Ref. [7]), 5.31 (Ref. [12]), 6 (Refs. [13] and [45]), 2.85 (Ref. [14]) and 3.0 (Ref. [46]) as shown in Table 2. However, the calculation by Yamamoto et al. [15] within the LDA framework caused a larger value of 7.5. This type of overestimation is also observed for other materials, such as HgI_2 [47]. The peak intensities of $\varepsilon_1(E)$ again differ between experiment and our calculation.

The calculated optical reflectivity and experimental data taken from Ref. [7] are shown in Fig. 4. The calculated reflectivity starts at about 18.89% and has a maximum value of roughly 36.84% at about 3.2 eV. The experimental reflectivity is 24% at 3.66 eV (Ref. [7]). Therefore, our result reproduces the positions of the peaks determined by inter-band transitions with good accuracy.

3.3. Phonon dispersion and phonon density of states

The calculated phonon dispersion relations along the Γ-X-U(K)-Γ-L-X-W-L direction of high symmetry in the first Brillouin zone are presented in Fig. 5. Since there are three atoms in the primitive cell, there are three acoustic modes and six optical modes. According to the symmetry analysis (crystal point group: O_h), the optical modes at the Γ point can be classified into the following symmetry species:

$$\Gamma_{\text{opt}} = T_{2g}(R) + T_{1u}(I), \tag{5}$$

where the notations R and I mean Raman active and infrared active modes, respectively. Both $T_{2g}(R)$ and $T_{1u}(I)$ are threefold degeneration. The other threefold degeneration T_{1u} mode is the acoustic mode. However, note that the degeneracy of the optical T_{1u} is partially lifted due to the LO-TO splitting.

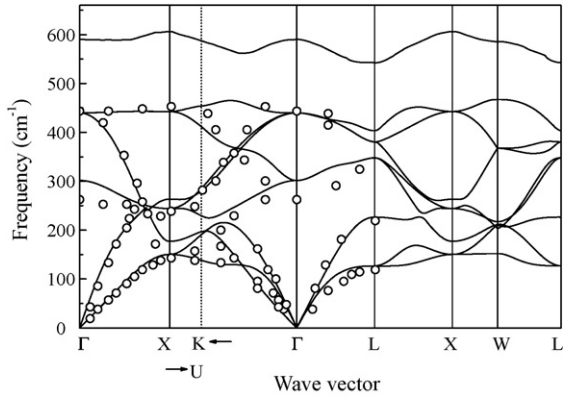

Fig. 5. Calculated phonon dispersion curves for CeO_2 along several lines of high symmetry in the first Brillouin zone. The discrete open circles represent the neutron data taken from Ref. [14].

The calculated Γ point Raman and infrared phonon frequencies together with other theoretical and experimental ones are summarized in Table 2. The agreement between the theoretical results and experimental data is good for the Raman and the T_{1u}(LO) modes. On comparison with the experimental frequency reported in Refs. [12–14], our calculated T_{1u}(TO) mode frequency is about 9% higher. The T_{1u}(TO) mode frequency reported by Ref. [7] seems to be too low compared to the infrared data of Refs. [12–14] as well as our calculated result. A similar overestimation of the T_{1u}(TO) branch has been observed in previous first-principles calculations of other fluorite structures such as PbF_2 [48], BaF_2 [48], and at the Γ point of CeO_2 [15].

For the convenience of further comparison with the experiment, the neutron scattering results by Clausen et al. [14] which contain only the frequencies below 500 cm^{-1} along the Γ-X-U(K)-Γ direction, are presented in Fig. 5 together with the calculated phonon dispersion curves. It can be seen that our calculated frequencies are in overall agreement with the experimental ones. In spite of the deviation of 9% for the T_{1u}(TO) branch at the Brillouin zone central Γ point of CeO_2, the agreement becomes better towards X and L points at the Brilloun zone boundary. Another feature in the phonon dispersion curves is the near-flatness of the T_{1u}(LO) branch, which is also observed in other fluorites structures [48].

4. Conclusion

Bonding, optical and lattice dynamical properties of CeO_2 have been investigated using the first-principles density-functional theory taking into account the on-site Coulomb interaction within the LDA + U scheme. The calculated dielectric constants, Born effective charge tensors, phonon dispersion curves agree well with the available experimental data. The analysis of the charge-density and electron-localization function distributions indicates that the Ce-O bonding nature in CeO_2 is covalent bond.

Acknowledgments

The present work is supported by National Natural Science Key Foundation of China (NSFC) (No. 50730004), National Natural Science Foundation of China (NSFC) (No. 50802089), Opening Project of State Key Laboratory of High Performance Ceramics and Superfine Microstructure (No. SKL200805SIC), Qianjiang Talent Project of Zhejiang Province (No. 2007R10028), and Science Foundation of Zhejiang Province (No. Y407188).

References

[1] S. Park, J.M. Vohs, R.J. Gorte, Nature (London) 404 (2000) 265.
[2] M.S. Dresselhaus, I.L. Thomas, Nature (London) 414 (2001) 332.
[3] F. Esch, S. Fabris, L. Zhou, T. Montini, C. Africh, P. Fornasiero, G. Comelli, R. Rosei, Science 309 (2005) 752.
[4] Q. Fu, H. Saltsburg, M. Flytzani-Stephanopoulos, Science 301 (2003) 935.
[5] G.A. Deluga, J.R. Salge, L.D. Schmidt, X.E. Verykios, Science 303 (2004) 993.
[6] T. Inoue, Y. Yamamoto, S. Koyama, S. Suzuki, Y. Ueda, Appl. Phys. Lett. 56 (1990) 1332.
[7] M. Marabelli, P. Wachter, Phys. Rev. B 36 (1987) 1238.
[8] A. Fujimori, Phys. Rev. B 27 (1983) 3992.
[9] F.L. Normand, J.E. Fallah, L. Hiliaire, P. Légaré, A. Kotani, J.C. Parlebas, Solid State Commun. 71 (1989) 885.
[10] E. Wuilloud, B. Delley, W.-D. Schneider, Y. Baer, Phys. Rev. Lett. 53 (1984) 202.
[11] P.W. Anderson, Phys. Rev. 24 (1961) 41.
[12] S. Mochizuki, Phys. Status Solidi B 114 (1982) 189.
[13] N.I. Santha, M.T. Sebastian, P. Mohanan, N.M. Alford, K. Sarma, R.C. Pullar, S. Kamba, A. Pashkin, P. Samukhina, J. Petzelt, J. Am. Ceram. Soc. 87 (2004) 1233.
[14] K. Clausen, W. Hayes, J.E. Macdonald, R. Osborn, P.G. Schnabel, M.T. Hutchings, A. Magerl, J. Chem. Soc. Faraday Trans. 283 (1987) 1109.
[15] T. Yamamoto, H. Momida, T. Hamada, T. Uda, T. Ohno, Thin Solid Films 486 (2005) 136.
[16] P.E. Blöchl, Phys. Rev. B 50 (1994) 17953.
[17] G. Kresse, J. Furthmüller, Phys. Rev. B 54 (1996) 11169.
[18] G. Kresse, D. Joubert, Phys. Rev. B 59 (1999) 1758.
[19] J.P. Perdew, A. Zunger, Phys. Rev. B 23 (1981) 5048.
[20] S.L. Dudarev, G.A. Botton, S.Y. Savrasov, C.J. Humphreys, A.P. Sutton, Phys. Rev. B 57 (1998) 1505.
[21] J.L.F.D. Silva, M.V. Ganduglia-Pirovano, J. Sauer, V. Bayer, G. Kresse, Phys. Rev. B 75 (2007) 045121.
[22] S. Fabris, S. de Gironcoli, S. Baroni, G. Vicario, G. Balducci, Phys. Rev. B 72 (2005) 237102.
[23] M. Cococcioni, S. de Gironcoli, Phys. Rev. B 71 (2005) 035105.
[24] P. Wachter, in: P. Wachter, H. Boppart (Eds.), Valence Instabilities, North-Holland, Amsterdam, 1982, p. 145.
[25] H.J. Monkhorst, J.D. Pack, Phys. Rev. B 13 (1976) 5188.
[26] M. Methfessel, A.T. Paxton, Phys. Rev. B 40 (1989) 3616.
[27] P.E. Blöchl, O. Jepsen, O.K. Andersen, Phys. Rev. B 49 (1994) 16223.
[28] K. Parlinski, Z.Q. Li, Y. Kawazoe, Phys. Rev. Lett. 78 (1997) 4063.
[29] K. Kunc, R. Martin, Phys. Rev. Lett. 48 (1982) 406.
[30] N.V. Skorodumova, R. Ahuja, S.I. Simak, I.A. Abrikosov, B. Johansson, B.I. Lundqvist, Phys. Rev. B 64 (2001) 115108.
[31] Z. Yang, T.K. Woo, M. Baudin, K. Hermansson, J. Chem. Phys. 120 (2004) 7741.
[32] T. Gürel, R. Eryiğit, Phys. Rev. B 74 (2006) 014302.
[33] L. Gerward, J.S. Olsen, L. Petit, G. Vaitheeswaran, V. Kanchana, A. Svane, J. Alloys Compd. 400 (2005) 56.
[34] C.J. Pickard, B. Winkler, R.K. Chen, M.C. Payne, M.H. Lee, J.S. Lin, J.A. White, V. Milman, D. Vanderbilt, Phys. Rev. Lett. 85 (2000) 5122.
[35] A. Nakajima, A. Yoshihara, M. Ishigame, Phys. Rev. B 50 (1994) 13297.
[36] L. Gerward, J.S. Olsen, Powder Diffr. 8 (1993) 127.
[37] S.J. Duclos, Y.K. Vohra, A.L. Ruoff, A. Jayaraman, G.P. Espinosa, Phys. Rev. B 38 (1988) 7755.
[38] J.P. Poirier, Introduction to the Physics of the Earth's Interior, 2nd ed., Cambridge University Press, New York, 2000.
[39] Z. Hu, R. Meier, C. Schübler-Langeheine, E. Weschke, G. Kainde, I. Felner, M. Merz, N. Nücker, S. Schupper, A. Erb, Phys. Rev. B 60 (1999) 1460.
[40] D.D. Koelling, A.M. Boring, J.H. Wood, Solid State Commun. 47 (1983) 227.
[41] N.V. Skorodumova, S.I. Simak, B.I. Lundqvist, I.A. Abrikosov, B. Johansson, Phys. Rev. Lett. 89 (2002) 166601.
[42] B. Silvi, A. Savin, Nature (London) 371 (1994) 683.
[43] R.D. King-Smith, D. Vanderbilt, Phys. Rev. B 47 (1993) 1651.
[44] R. Resta, Rev. Mod. Phys. 66 (1994) 899.
[45] S. Guo, H. Arwin, S.N. Jacobsen, K. Järrendahl, U. Helmersson, J. Appl. Phys. 77 (1995) 5369.
[46] M. Niwano, S. Sato, T. Koide, T. Shidara, A. Fujimori, H. Fukutani, S. Shin, M. Ishigame, J. Phys. Soc. Jpn. 57 (1988) 1489.
[47] R. Ahuja, S. Auluck, O. Eriksson, J.M. Wills, B. Johansson, Phys. Rev. B 54 (1996) 10419.
[48] A. Dubinin, B. Winkler, K. Knorr, V. Milman, Eur. J. Biochem. 39 (2004) 27.